Journal of Biomedical Optics

BiomedicalOptics.SPIEDigitalLibrary.org

Noncontact photoacoustic tomography of *in vivo* chicken chorioallantoic membrane based on all-fiber heterodyne interferometry

Jonghyun Eom
Seong Jun Park
Byeong Ha Lee

SPIE.

Noncontact photoacoustic tomography of *in vivo* chicken chorioallantoic membrane based on all-fiber heterodyne interferometry

Jonghyun Eom,[a] Seong Jun Park,[b] and Byeong Ha Lee[c,*]
[a]Gwangju Institute of Science and Technology, Department of Medical System Engineering, 123 Cheomdan-gwagiro, Buk-gu, Gwangju 500-712, Republic of Korea
[b]Institute for Basic Science, Center for Soft and Living Matter, 50 UNIST-gil, Ulju-gun, Ulsan 689-798, Republic of Korea
[c]Gwangju Institute of Science and Technology, School of Information and Communications, 123 Cheomdan-gwagiro, Buk-gu, Gwangju 500-712, Republic of Korea

Abstract. We present three-dimensional (3-D) *in vivo* photoacoustic (PA) images of the blood vasculature of a chicken chorioallantoic membrane (CAM) obtained by using a fiber-based noncontact PA tomography system. With a fiber-optic heterodyne interferometer, the system measures the surface displacement of a sample, induced by the PA wave, which overcomes the disadvantage of physical-contact of ultrasonic transducer in a conventional system. The performance of an implemented system is analyzed and its capability of *in vivo* 3-D bioimaging is presented. At a depth of 2.5 mm in a phantom experiment, the lateral and axial resolutions were measured as 100 and 30 μm, respectively. The lateral resolution became doubled at a depth of 7.0 mm; however, interestingly, the axial resolution was not noticeably deteriorated with the depth. With the CAM experiment, performed under the American National Standards Institute laser safety standard condition, blood vessel structures placed as deep as 3.5 mm were clearly recognized. [DOI: 10.1117/1.JBO.20.10.106007]

Keywords: photoacoustic tomography; noncontact detection; fiber optic imaging; heterodyne interferometer; surface displacement.
Paper 150410RR received Jun. 19, 2015; accepted for publication Sep. 22, 2015; published online Oct. 16, 2015.

1 Introduction

Photoacoustic tomography (PAT), as a powerful noninvasive imaging modality, allows structural and functional imaging of biological tissues, and opens new applications in many biomedical and clinical fields.[1–4] PAT relies on the PA effect, relating the optical energy absorption at a point in a sample with the acoustic wave generated by the thermal expansion of that point.[5] This hybrid technique of optical absorption and ultrasound generation provides good optical contrast and high-ultrasonic resolution at depths of up to several centimeters,[2] so that various biological studies from organelles to organs such as cells, blood vessels, small animal brains, and full organs have been reported, and they have supplied useful information pertinent to specific diseases and cancers.[1–4]

In PA imaging, the acoustic wave excited in a depth propagates to the sample surface, where it is detected by either a mechanically scanned single-element ultrasonic transducer or an array-type ultrasonic transducer. Assuming that thermomechanical properties and acoustic parameters are distributed homogeneously in a sample, the PA image of the sample, depending on the distribution of absorbers, can be reconstructed from the time-resolved PA signals.[1–4] For the detection of acoustic signals, a conventional PAT system usually uses an ultrasonic transducer made with piezoelectric material (PZT). However, the PZT requires physical contact with the sample, which gives rise to some obstacles in biomedical imaging. The contact-based detection scheme should be avoided in many applications such as burn diagnostics,[6] brain surgery,[7] and ophthalmology[8] because the physical contact might cause secondary infections. Furthermore, the opaque PZT restricts the illumination direction of the excitation laser beam, so that inline configuration of the ultrasonic transducer and the laser is not easy. It is also difficult to combine the PAT system with other optical imaging systems such as optical coherent tomography (OCT) or fluorescence imaging due to the difference in the types of detection schemes.[9,10]

Optical interferometric methods have been reported as alternatives to PZT-based transducers.[11–22] Mach–Zehnder interferometer,[11–14] low-coherence Michelson interferometer,[15] and Fabry–Perot interferometer[16–19] were used for the detection of acoustic signals. These techniques have difficulties for practical applications, however, because they are implemented with bulky and complicated optics in general,[12,13] or demand an impedance matching liquid layer on top of the sample.[15] One group[14] has utilized fiber-optics for a compact and flexible system, but the probe part for collecting the back-reflected light was still composed of bulk optics. To avoid the blocking of the beam path of the excitation laser, caused mainly by the opaqueness of a conventional ultrasonic transducer, optically transparent polymer film-based Fabry–Perot sensors[17–19] and fiber-optic sensors[20–22] have been proposed. However, they still required either direct contact with the biological sample or water immersion for impedance matching. In addition, these bulky and complicated optics and contact-based detection impose constraints on implementing multimodal imaging systems.[23,24]

Recently, we have introduced a noncontact PAT system using an optical fiber interferometer, where bulk optics were replaced

*Address all correspondence to: Byeong Ha Lee, E-mail: leebh@gist.ac.kr

with compact fiber optics including a lensed fiber, and confirmed the feasibility with a simple phantom experiment.[25] The system extracted the acoustic pressure from the surface displacement that was detected with the optical interferometer. However, to get more realistic imaging of various biological samples, we needed to improve the system in several aspects including the quantitative evaluation of imaging performance, the laser safety of the detection beam, and the uniform illumination of the excitation laser beam.

In this paper, we present and analyze the performance of a noncontact PAT system, which has been modified and improved from our previous system[25] for biomedical tissue imaging. To comply with laser safety[26] of biological samples, the size of the interrogating laser beam is expanded by adjusting the curvature of the lensed fiber. The excitation laser beam is aligned uniformly and perpendicularly to illuminate the sample. The lateral resolution of the system is measured by using a sample in a wedge shape and finding the minimum discernible gap distance. The axial resolution is measured in terms of the imaging depth by using the phantom having several targets in different depths. The capability of multidimensional imaging of the system is demonstrated by presenting two and three-dimensional (3-D) PA images of tissue mimicking phantoms and showing *in vivo* images of the blood vasculature of a chicken chorioallantoic membrane (CAM).

2 Materials and Methods

2.1 *Experimental Setup*

The schematic of the noncontact PAT system is depicted in Fig. 1, which has been modified for biomedical tissue imaging from our previous work.[25] The system consists of two parts: excitation part and detection part. In the excitation part, a Q-switched Nd:YAG laser (Quantel, Brilliant ultra 50) is used to excite the acoustic pressure waves within the sample. It emits a train of 8-ns duration pulses at a 532-nm wavelength with a repetition rate of 20 Hz and a maximum energy of 50 mJ per pulse. The optical energy of the laser pulse can be adjusted by rotating a half-wave plate. The excitation beam, upon passing through a beam splitter, is split into two ways to allow rather uniform excitation. Both beams are aligned to perpendicularly illuminate the sample.

The detection part consists of a fiber-optic heterodyne interferometer (FHI) to measure the surface displacement of the sample induced by the PA waves. The interferometer is implemented using a single frequency laser (Thorlabs, SFL 1550s) with a low-linewidth of 50 kHz and a 1550-nm center wavelength. The laser power is adjusted with a current driver (Thorlabs, ITC 510) to comply with the laser's safety limit.[26] The laser beam is split into a reference path and a detection path by the first 50:50 coupler. The reference beam is frequency-modulated with an acousto-optic modulator (AOM; Gooch & Housego, Fiber-Q FCAOM), driven by an AOM driver at 80 MHz, and directed to the second 50:50 coupler through a polarization controller (Thorlabs, FPC031). The detection beam of the FHI is guided onto the sample surface through an optical fiber circulator (Fiberpi Co. Ltd., h031) and a homemade lensed fiber. An optical fiber filter (Fiberpi Co. Ltd., of060) is used to protect and isolate the detection part from the strong excitation beam. The lensed fiber shown in Fig. 1 is fabricated by splicing a single mode lead fiber with a short piece of coreless silica fiber (CSF) and then by arc-discharging the other end of the CSF piece.[27] Two lensed fibers were fabricated with working distances of 0.91 and 2.5 mm, and minimum beam widths of 10 and 62 μm, respectively.

The detection beam, which is focused onto the sample surface and phase-shifted by the acoustic pressure waves, is recoupled into the same probe through the lensed fiber. The probe head is mounted on an $X-Y$ motorized translation stage (Newport Co., PM-500) to acquire dimensional images. The reference beam and the detection beam are recombined and interfered with each other after passing through the second coupler. The interference is detected by a balanced photodetector (Thorlabs, PDB430C). The interference signals

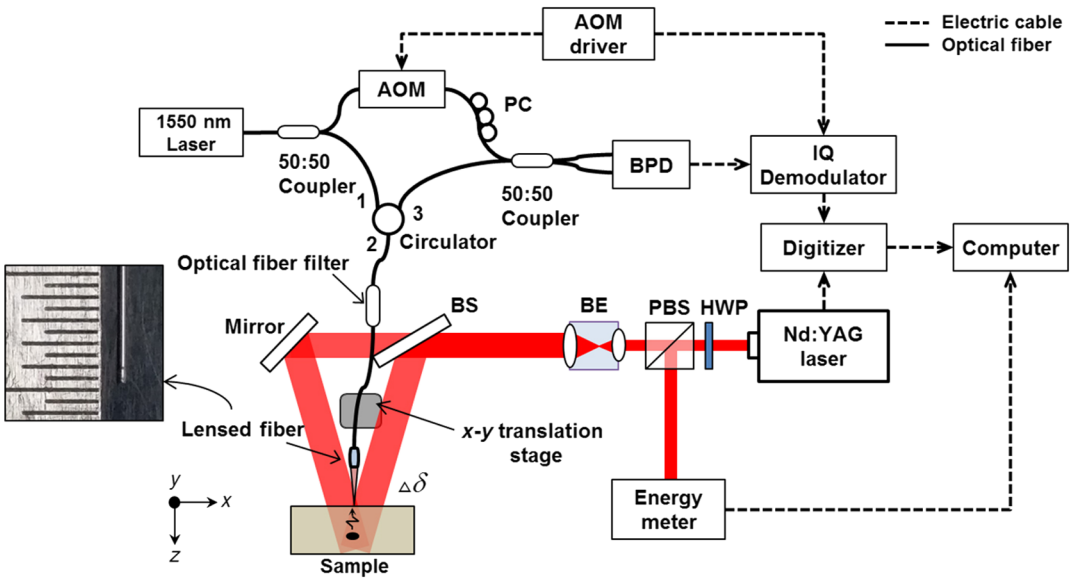

Fig. 1 Schematic of the noncontact photoacoustic tomography setup. AOM, acousto-optic modulator; PC, polarization controller; BPD, balanced photo detector; BS, beam splitter; BE, beam expander; PBS, polarizing beam splitter; HWP, half-wave plate. (inset: photograph of the lensed fiber with a 1 mm-scale ruler).

are demodulated with the AOM driving signal using a self-built in-phase and quadrature (IQ) demodulator, and the two demodulated signals are captured with a high-speed digitizer (National Instruments, NI-5142). A personal computer programmed with LabVIEW (National Instruments) controls the $X-Y$ translation stage through a GPIB connection and reconstructs the PA image via the Fourier transform–based reconstruction algorithm.[28,29]

2.2 *Principle of Acoustic Pressure Measurement*

To extract the surface displacement from the interference signals, we have built the IQ demodulator as shown in Fig. 1. When the reference beam modulated by AOM and the detection beam are recombined, the interference signal is given as

$$I_1(t) = A_1 \cos[2k\Delta\delta(t) + \omega_M t], \tag{1}$$

where A_1 is the signal amplitude, k is the wavenumber of the light source, $\Delta\delta(t)$ is the time-varying displacement of the sample surface induced by the acoustic wave, and ω_M is the angular frequency of the AOM. For the IQ signal demodulation, the signal of Eq. (1) is multiplied with the in-phase (I) AOM driving signal

$$I_2(t) = A_2 \cos(\omega_M t), \tag{2}$$

and with its quadrature phase-shifted (Q) one. After low-pass filtering, we have two demodulated signals, the in-phase I and the quadrature Q, as $A_{12}\cos[2k\Delta\delta(t)]$ and $A_{12}\sin[2k\Delta\delta(t)]$, respectively. Then the surface displacement is simply calculated by taking the arctangent between the two demodulated signals as

$$\Delta\delta(t) = \frac{1}{2k}\tan^{-1}\left\{\frac{\sin[2k\Delta\delta(t)]}{\cos[2k\Delta\delta(t)]}\right\}. \tag{3}$$

The corresponding acoustic pressure $p(t)$ can be obtained by taking the time derivative of the surface displacement,[30]

$$p(t) = \frac{Z}{2}\frac{\partial\Delta\delta(t)}{\partial t}, \tag{4}$$

where Z is the acoustic impedance of the medium (about 1.5×10^6 Pa $\cdot$ s/m for soft tissues), and the acoustic pressure wave is assumed to be a plane wave. Note that the scaling factor $1/2$ in Eq. (4) represents the free boundary condition at the air–sample interface. After acquiring the acoustic wave signals from the surface displacement, the PA image as the initial pressure distribution is reconstructed by using the Fourier-transform reconstruction algorithm.[28,29]

2.3 *Sample Preparation*

For evaluating the proposed system, we have prepared two types of tissue-mimicking phantoms and one animal model. To make a gelatin-based tissue-mimicking phantom, black polyethylene terephthalate (PET) fibers (HellermannTyton, BSHLR180) with diameters of 200 and 150 μm were used as light-absorbers. At first, gelatin powder [J.T. Baker, NF(Type B)] was stirred into distilled water at 40°C until completely dissolved. The concentration of gelatin solution was about 10% weight fraction, and one gram per liter of TiO_2 (JUNSEI, rutil form) was added as optical scattering particles. Before the solidification of the gelatin solution, PET fibers were loaded in the solution. Finally, the solution was placed into a refrigerator to solidify. This gelatin-based phantom has a reasonable cost and long temporal stability, and the fabrication process is straightforward.[31] For the second tissue-mimicking phantom, we used a 5% solution of milk diluted with water and black PET fibers. The milk solution is generally used to mimic a scattering medium such as biological tissue, because the main components of milk are fat and protein.[32] For all phantom imaging, the fluence of Q-switched Nd:YAG laser was 10 mJ/cm^2, the power of the detection beam was 1 mW, and the working distance and the spot size of the lensed fiber were 0.91 mm and 10 μm, respectively.

For the animal model, we used a chicken CAM vasculature, which provided easy access to a well-developed vasculature. For the development of blood vessels, fertilized chicken eggs were incubated at 37°C for 10 days. After checking the blood vessel structure formation, the upper shell of the egg was carefully removed for imaging. For CAM imaging, the Q-switched Nd:YAG laser was used with a beam diameter of 15 mm and fluence of 10 mJ/cm^2. A detection beam of 0.1 mW and the lensed fiber of working distance of 2.5 mm and spot size of 62 μm were used.

3 Results and Discussion

3.1 *Measurement of Photoacoustic Signal from Surface Displacement*

The measurement capabilities of the proposed FHI were experimentally evaluated using the tissue-mimicking gelatin phantom, containing two black PET fibers with a diameter of 200 μm and a length of 2 mm. The two PET fibers were spaced 1.2 mm apart and placed at different depths of 2 and 3.2 mm in the phantom, as shown in the inset of Fig. 2(a). The probe beam of FHI was positioned perpendicularly above the first PET fiber embedded at a depth of 2 mm. Figure 2(a) shows the measured surface displacement. In the figure, the gradual thermal expansion of the phantom can be observed just after the pulse firing at 8 μs, which is thought to be due to the background optical absorption by the phantom.[13] The two peaks, "a" at 9.38 μs and "b" at 10.19 μs, indicate the surface displacement induced by the two acoustic pressure waves coming from the two black PET fibers. The acoustic pressure of Fig. 2(b) was obtained by differentiating the surface displacement of Fig. 2(a). In general, there is random noise in the measurement of Fig. 2(a), which could be amplified due to the differentiation of Eq. (4). In order to reduce the random noise, we used a median filter with a window size of four. Two bipolar signals "a′" and "b′" indicate that the PA signals are clearly distinguished from the noise. The time delay between peak a′ and peak b′ is caused by the difference depths of the PET fibers in the phantom.

To evaluate the displacement resolution of FHI, we measured the surface displacement during a time span of 25 μs without laser excitation and calculated the standard deviation of the signal amplitude. We found that the standard deviation of the signal amplitude fluctuation was about 0.5 nm corresponding to 18.7 kPa, which is thought to be low enough to measure the surface displacement induced by acoustic waves. As usual, the system resolution could be further improved by repeating the measurements and averaging many measured signals.

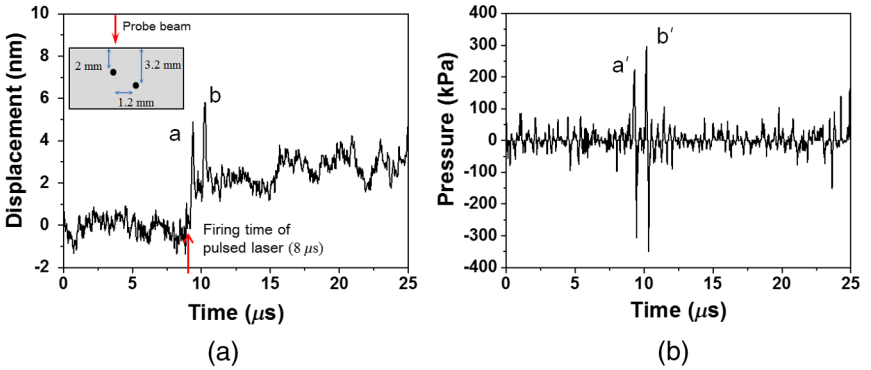

Fig. 2 Photoacoustic signal detected from a phantom containing two black polyethylene terephthalate (PET) fibers. (a) The time-resolved surface displacement (inset: the experimental phantom structure). (b) The acoustic pressure corresponding to the displacement; the firing time of the pulsed laser is 8 μs.

3.2 *Evaluation of Image Resolution Limit*

To evaluate the resolution limit of the reconstructed image, we used two PET fibers of 200-μm diameter submerged in the 5% mixture of milk and water at a depth of 2.5 mm. Figure 3(a) shows the top view of the phantom schematic; two PET fibers are placed on a Petri dish in a wedge shape. The PA signals coming from the PET fibers were measured as the probe scanned a length of 8 mm in the direction of each arrow. Figures 3(b)–3(d) show the reconstructed PA images obtained at different locations where the distance between two PET fibers was 0, 50, and 200 μm, respectively. Their lateral profiles are depicted in each reconstructed image. The PET fibers with the 50 μm spacing are seen as one structure, but with the 200 μm spacing they are clearly distinguished.

To determine the minimum discernible distance between PET fibers, referred to as the lateral resolution, additional experiments have been carried out in the range from 50 to 200 μm spacings. Figure 4 shows the PA image obtained with the PET fibers of 100-μm spacing. The reconstructed two-dimensional (2-D) image in Fig. 4(c) agrees well with the PET fibers as described in Fig. 4(b), and the lateral and axial profiles of the reconstructed image are presented in Figs. 4(a) and 4(d), respectively. For evaluation of the spatial resolution, we used the Rayleigh's resolution criterion, in which two individual objects are resolved when their overlapped intensity at the saddle point is below 81% of the maximum intensity.[33] In the lateral profile shown in Fig. 4(a), the acoustic pressure intensity at the saddle point is about 75% of the maximum intensity; thus, it satisfies the Rayleigh's criterion. Therefore, we can say that our system provides a lateral resolution of better than 100 μm. Meanwhile, the axial profile depicted in Fig. 4(d) shows that a full width at half maximum (FWHM) is about 230 μm. This value is similar to the actual diameter of each PET fiber, 200 μm, thus allowing us to estimate that the axial resolution is ~30 μm. The theoretical axial resolution can be estimated as $0.88v/B$, where v is the speed of sound (1540 m/s in water or tissue) and B is the detection bandwidth.[34] Since the detection bandwidth of our system is 50 MHz, the theoretical axial resolution is approximately 27.1 μm. This value is well matched to the experimentally estimated one of ~30 μm.

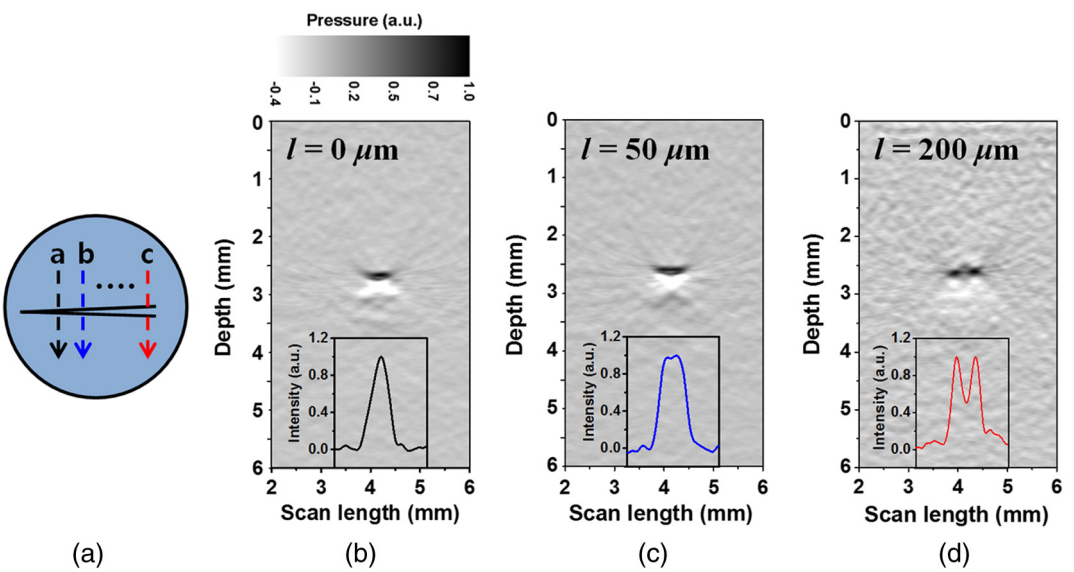

Fig. 3 (a) Top view of the schematic of the PET fiber phantom. (b)–(d) Reconstructed photoacoustic images and their lateral profiles scanned PET fibers phantom at "a," "b," and "c" locations at which the distance (l) between the two PET fibers are 0, 50, and 200 μm, respectively.

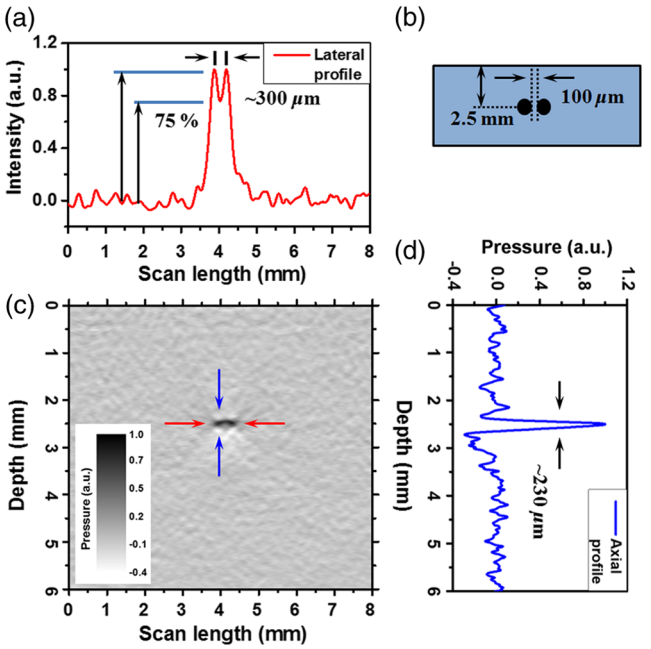

Fig. 4 Reconstructed image of the phantom containing two parallel PET fibers: (a) lateral profile of the reconstructed image; (b) schematic of the phantom containing two parallel PET fibers; (c) reconstructed image of the two PET fibers; and (d) axial profile of the reconstructed image.

To investigate the change of spatial resolution with the imaging depth, we have used a phantom containing five black PET fibers located at different depths. The PET fibers with a 150-μm diameter were placed into a container which was filled with the 5% solution of milk and water. The probe scan was made perpendicularly to the phantom surface along a line of 10-mm length in 50-μm steps. Figure 5(a) shows the reconstructed 2-D image of the PET fibers phantom. The PET fibers are clearly visible and well-distinguished, but the dimensions of the PET fibers are changed as the depth increases. For evaluation of the change, we have obtained the lateral and axial profiles of five PET fibers, indicated as A, B, C, D, and E in Fig. 5(a), which are normalized to the maximum pressure intensity in the image. Figures 5(b) and 5(c) are the lateral profiles and the axial profiles of PET fibers located at different depths, and Fig. 5(d) is the comparison of the FWHM of the profiles. With increasing depth, the FWHM of lateral profile increases, whereas the FWHM of the axial profile is maintained almost constant with a slight tendency to decrease. In general, the lateral resolution is limited by the imaging depth when the detection bandwidth, detection beam size, and scanning length are fixed. On the other hand, the axial resolution is not appreciably dependent on the imaging depth.[29,35]

3.3 *Three-Dimensional Imaging of Phantom*

We have investigated the capability of multidimensional imaging by using a phantom composed of black PET fibers immersed in a 5% solution of milk and water. Figure 6(a) is the scheme of the phantom and its photograph. Two black PET fibers, each with a 200-μm diameter, were placed into a container at different heights and fixed with a double-sided tape, but one of them was twisted into a loop. After pouring the milk solution in the container, the probe was scanned over an area of 9 mm $\times$ 9 mm in steps of 100 μm. Figure 6(b) shows the maximum intensity projections (MIP) of the 3-D PA image reconstructed along the XY, YZ, and XZ planes. Both the straight PET fiber and the twisted PET fiber are clearly recognized and well-matched with the phantom schematic. However, at the places where the PET fibers are overlapped we can see some faded regions as in the XY plane image of Fig. 6(b).

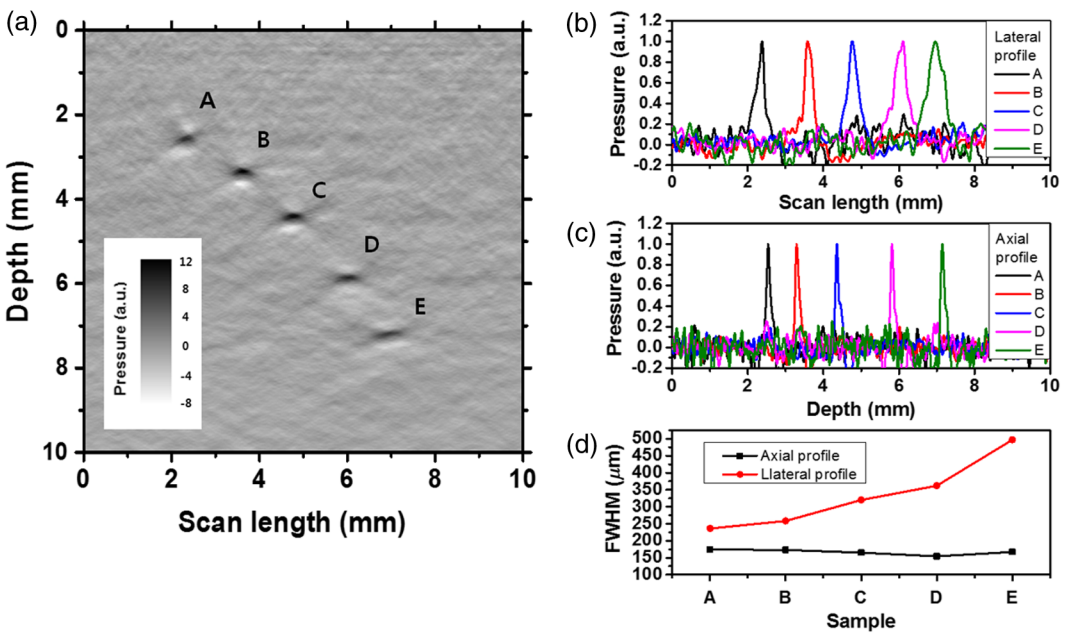

Fig. 5 (a) Reconstructed image of the phantom containing five PET fibers, (b) lateral profiles (normalization) and (c) axial profiles (normalization) of the PET fibers in the image (a), (d) FWHM of lateral and axial profiles of the five PET fibers.

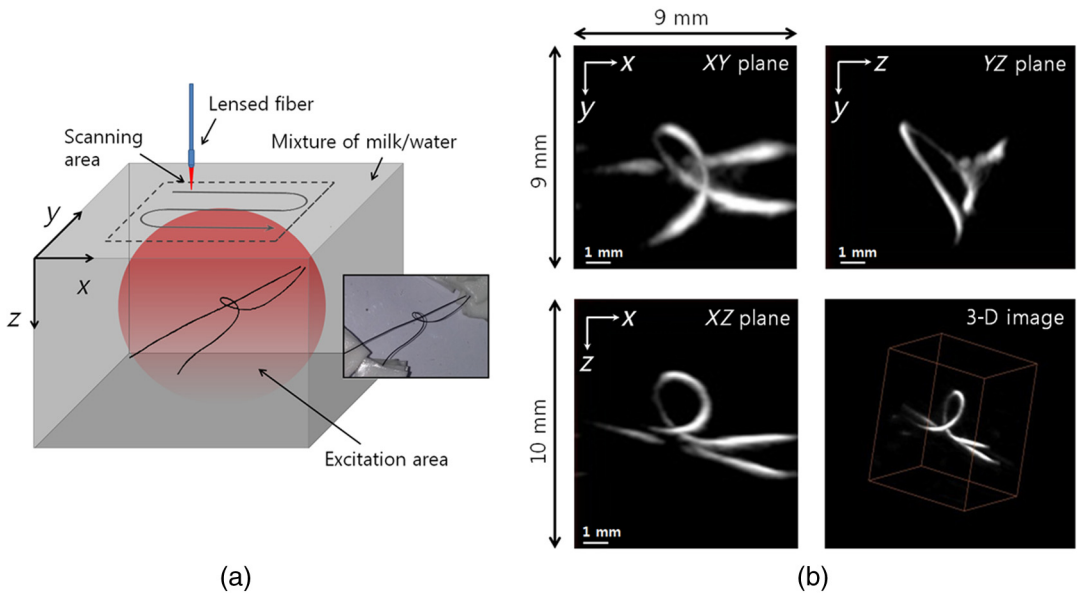

Fig. 6 (a) Schematic of the PET fibers phantom (inset: photograph of the PET fibers), and (b) PA images of the phantom. Top left: *XY* plane maximum intensity projection image (MIP) of a three-dimensional (3-D) PA image. Top right: *YZ* plane MIP image. Lower left: *XZ* plane MIP image. Lower right: 3-D image (Video 1, MPEG, 5.9 MB) [URL: http://dx.doi.org/10.1117/1.JBO.20.10.106007.1].

3.4 *Three-Dimensional Imaging of Chicken Chorioallantoic Membrane Vasculature*

Chicken CAM vasculature was used as a sample for *in vivo* imaging to evaluate the applicability of the noncontact PA imaging to biomedical samples. Figure 7(a) is a photograph of the blood vessel network of the CAM, which is covered by transparent albumen (egg white). To excite the PA waves, the Q-switched Nd:YAG laser was used with a beam diameter of 15 mm and fluence of 10 mJ/cm^2, which complies with the American National Standards Institute (ANSI) laser safety standard of 20 mJ/cm^2.[26] The energy density of the probe beam, focused on the surface of the albumen through the lensed fiber, was 0.165 J/cm^2, which complies with the maximum permissible exposure (MPE) in the ANSI laser safety standard. Note that the MPE value for skin at a 1550 nm wavelength is 1 J/cm^2.[26] PA signals were measured by scanning the probe beam over an area of 8 mm × 7.5 mm in steps of 50 μm. The probe beam was nearly perpendicular to the surface of the albumen, and 10 signals per each position were averaged. Figure 7(b) shows the MIP images and the reconstructed 3-D video image. The blood vessels placed at 3.5 mm under the surface are clearly recognized. In particular, the MIP image of the *XY* plane is well matched with the photograph in Fig. 7(a). In the upper right area of the reconstructed PA image, the blurred background signals are shown in nearby blood vessels. These background signals are thought as being originated from lutein and zeaxanthin pigments in the egg yolk. Because their absorption wavelength is in the visible light band, they can be observed in the PA image.[36]

We calculated the contrast-to-noise ratio (CNR) of the MIP (*XY* plane) image, defined as[11]

$$\mathrm{CNR}_{\mathrm{ROI}} = \frac{I_{\mathrm{ROI}} - I_{\mathrm{bg}}}{\sigma_{\mathrm{bg}}}, \tag{5}$$

where I_{ROI} is the mean intensity within the region of interest (ROI), and I_{bg} and σ_{bg} represent the mean and standard deviation acoustic intensity in the background region. As was marked in the *XY* plane image of Fig. 7(b), four ROIs were considered. The noise was assumed to be uniformly distributed, and ROI 5 was chosen to get the background noise. With Eq. (5), CNRs were calculated as $\mathrm{CNR}_{\mathrm{ROI1}} = 16.5$, $\mathrm{CNR}_{\mathrm{ROI2}} = 22.3$, $\mathrm{CNR}_{\mathrm{ROI3}} = 41.4$, and $\mathrm{CNR}_{\mathrm{ROI4}} = 20.2$.

In general, CNR is influenced by the radiant energy of the pulsed laser; thus, the applied optical fluence of 10 mJ/cm^2 can be said to be high enough to distinguish the blood vessels in the CAM image. Since the PA signal is proportional to the amount of energy absorbed by the sample, the most effective and simplest way of getting a high CNR is increasing the pulse energy. In addition, increasing the exposure time of the laser helps the CNR by increasing the amount of signal as long as the stress confinement is maintained. However, an average of the measured signals is required, which could consume the signal processing time.[37]

In most of our experiments, the PA signals were measured at flat and reflective surfaces, and the probe beam of the interferometer was aligned perpendicularly to the surface. However, in real biological applications, we can think of the signal as suffering from the surface roughness of samples. To overcome the signal degradation and/or distortion caused by the sample surface roughness, several studies have been made.[15,38,39] Additional materials such as water or oil were applied on the sample surface to increase its reflectance and/or reduce the roughness.[15] A photorefractive crystal was also used to concentrate the beam scattered from the rough surface.[38,39] In the proposed system, we will be able to improve its limitations by applying the surface smoothing materials as in the reported study[15] or compensate the image distortion by measuring the roughness of the sample before the PA measurement. In addition, an important issue for biological imaging is the imaging speed. In our current configuration, unfortunately, the imaging speed was highly limited by the low-repetition rate of the pulsed laser; it was only 20 Hz. Therefore, when we got one sheet of a 2-D depth image under the experimental conditions of 1 cm scan

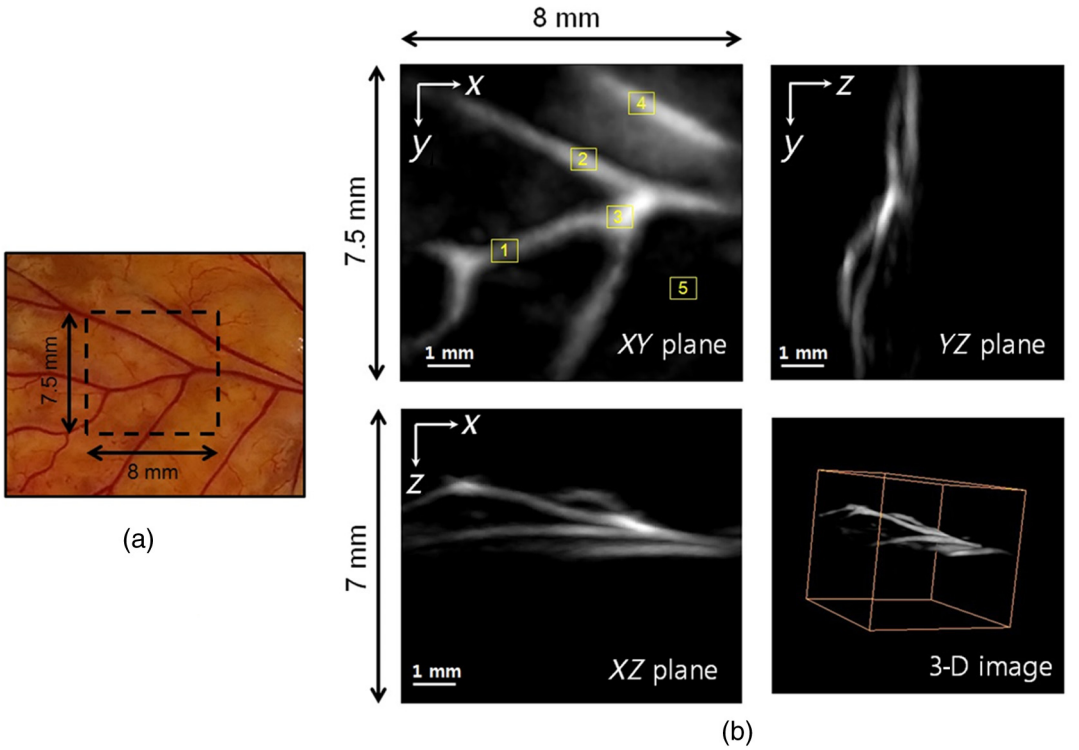

Fig. 7 (a) Photograph of blood vessels on chicken chorioallantoic membrane (CAM). The dotted box indicates the scanning area, (b) 3-D photoacoustic images of the CAM. Top left: *XY* plane MIP image. Top right: *YZ* plane MIP image. Lower left: *XZ* plane MIP image. Lower right: 3-D image (Video 2, MPEG, 2.9 MB) [URL: http://dx.doi.org/10.1117/1.JBO.20.10.106007.2].

length and 100 steps, the data acquisition time was as poor as 5 s. For the real-time image reconstruction, the imaging acquisition speed should be higher than 10 fps in general. By using the laser with a repetition rate of 2 kHz, we can acquire the same data within 0.05 s, which enables to get more realistic 3-D images *in vivo*. Therefore, it is definitely necessary to use a laser with a higher repetition rate.

In our proposed system, the fiber-based detection part takes full advantage of the simplicity, compactness, and flexibility for PA signal detection. However, the excitation part is still in free-space. Thus, we are struggling to change the excitation part with fiber optics also. We can use commercial optical fibers to transmit the pulsed laser beam. However, launching a high-power pulsed laser to the fiber is not easy work, because it can melt the end of the fiber. Especially, in our case, we should send the excitation pulsed laser beam and the interrogation continuous wave beam in a line. The possibility may be utilizing the dual cladding fiber (DCF) and associated fiber optics.[40] We can send the high-power excitation beam through the inner cladding of the DCF and the rather low-power interrogating beam through the core of the same fiber. However, the proper DCF and related devices are not commercially available yet.

4 Conclusion

We have demonstrated and analyzed the performance of the noncontact PAT system implemented by using an all-fiber-optic interferometer as a PA signal detector. The proposed system successfully measured the PA signals from the surface of a sample without requiring any physical contact with the sample. It enabled to get multidimensional PA images of the tissue-mimicking phantoms and the *in vivo* blood vasculature of chicken CAM. The lateral resolution of the PA image was better than 100 μm at a depth of 2.5 mm, while the axial resolution was ~30 μm at the same depth. Interestingly, with the imaging depth, the lateral resolution was getting worse but the axial resolution was nearly the same. The proposed system could find applications in the fields where noninvasive, noncontact, or minimally invasive imaging is specifically required. Furthermore, we expect that the use of fiber-optic components in the system could be extended to endoscopic applications. We are planning to combine the proposed system with a fiber-based OCT system[41] or a fluorescence imaging system, which would be able to provide a variety of physiological information about delicate biomedical samples.

Acknowledgments

This work was supported by the BioImaging Research Center at the Gwangju Institute of Science and Technology, Republic of Korea.

References

1. X. Wang et al., "Noninvasive laser-induced photoacoustic tomography for structural and functional in vivo imaging of the brain," *Nat. Biotechnol.* **21**, 803–806 (2003).
2. L. V. Wang, "Multiscale photoacoustic microscopy and computed tomography," *Nat. Photonics* **3**, 503–509 (2009).
3. L. V. Wang and S. Hu, "Photoacoustic tomography: in vivo imaging from organelles to organs," *Science* **335**, 1458–1462 (2012).
4. C. Li and L. V. Wang, "Photoacoustic tomography and sensing in biomedicine," *Phys. Med. Biol.* **54**(19), R59–R97 (2009).
5. A. G. Bell, "On the production and reproduction of sound by light," *Am. J. Sci.* **s3-20**, 305–324 (1880).
6. J. P. Jones et al., *Acoustical Imaging*, Springer, New York (1997).

7. V. Ntziachristos, J. S. You, and G. M. van Dam, "Current concepts and future perspectives on surgical optical imaging in cancer," *J. Biomed. Opt.* **15**(6), 066024 (2010).
8. S. Jiao et al., "Photoacoustic ophthalmoscopy for in vivo retinal imaging," *Opt. Express* **18**, 3967–3972 (2010).
9. X. Zhang, H. F. Zhang, and S. Jiao, "Optical coherence photoacoustic microscopy: accomplishing optical coherence tomography and photoacoustic microscopy with a single light source," *J. Biomed. Opt.* **17**(3), 030502 (2012).
10. I. Kosik and J. J. L. Carson, "Combined 3D photoacoustic and 2D fluorescence imaging of indocyanine green contrast agent flow," *Proc. SPIE* **8581**, 858143 (2013).
11. S. A. Carp and V. Venugopalan, "Optoacoustic imaging based on the interferometric measurement of surface displacement," *J. Biomed. Opt.* **12**(6), 064001 (2007).
12. S. A. Carp et al., "Optoacoustic imaging using interferometric measurement of surface displacement," *Appl. Phys. Lett.* **85**, 5772–5774 (2004).
13. B. P. Payne et al., "Optoacoustic tomography using time-resolved interferometric detection of surface displacement," *J. Biomed. Opt.* **8**(2), 273–280 (2003).
14. A. Hochreiner et al., "Non-contact photoacoustic imaging using a fiber based interferometer with optical amplification," *Biomed. Opt. Express* **4**, 2322–2331 (2013).
15. Y. Wang, C. Li, and R. K. Wang, "Noncontact photoacoustic imaging achieved by using a low-coherence interferometer as the acoustic detector," *Opt. Lett.* **36**, 3975–3977 (2011).
16. G. Rousseau, A. Blouin, and J. P. Monchalin, "Non-contact photoacoustic tomography and ultrasonography for tissue imaging," *Biomed. Opt. Express* **3**(1), 16–25 (2012).
17. P. C. Beard, F. Perennes, and T. N. Mills, "Transduction mechanisms of the Fabry Perot polymer film sensing concept for wideband ultrasound detection," *IEEE Trans. Ultrason. Ferroelectr. Freq. Control* **46**(6), 1575–1582 (1999).
18. P. C. Beard, "Photoacoustic imaging of blood vessel equivalent phantoms," *Proc. SPIE* **4618**, 54–62 (2002).
19. E. Zhang, J. Laufer, and P. Beard, "Backward-mode multiwavelength photoacoustic scanner using a planar Fabry-Perot polymer film ultrasound sensor for high-resolution three-dimensional imaging of biological tissues," *Appl. Opt.* **47**, 561–577 (2008).
20. P. C. Beard et al., "An optical fibre photoacoustic-photothermal probe," *Opt. Lett.* **23**(15), 1235–1237 (1998).
21. Y. Miida and Y. Matsuura, "All-optical photoacoustic imaging system using fiber ultrasound probe and hollow optical fiber bundle," *Opt. Express* **21**, 22023–22033 (2013).
22. E. Z. Zhang and P. C. Beard, "A miniature all-optical photoacoustic imaging probe," *Proc. SPIE* **7899**, 78991F (2011).
23. E. Z. Zhang et al., "Multimodal photoacoustic and optical coherence tomography scanner using an all optical detection scheme for 3D morphological skin imaging," *Biomed. Opt. Express* **2**, 2202–2215 (2011).
24. S. L. Chen et al., "A fiber-optic system for dual-modality photoacoustic microscopy and confocal fluorescence microscopy using miniature components," *Photoacoustics* **1**, 30–35 (2013).
25. S. J. Park et al., "Noncontact photoacoustic imaging based on all-fiber heterodyne interferometer," *Opt. Lett.* **39**(16), 4903–4906 (2014).
26. I. J. White and H. D. Dederich, *American National Standard for Safe Use of Lasers ANSI Z136, 1–2007*, American National Standards Institute Inc., New York (2007).
27. S. Y. Ryu et al., "Lensed fiber probes designed as an alternative to bulk probes in optical coherence tomography," *Appl. Opt.* **47**(10) 1510–1516 (2008).
28. K. P. Kostli et al., "Temporal backward projection of optoacoustic pressure transients using Fourier transform methods," *Phys. Med. Biol.* **46**, 1863–1872 (2001).
29. K. P. Köstli and P. C. Beard, "Two-dimensional photoacoustic imaging by use of Fourier-transform image reconstruction and a detector with an anisotropic response," *Appl. Opt.* **42**, 1899–1908 (2003).
30. D. Royer and E. Dieulesaint, *Elastic Waves in Solids I: Free and Guided Propagation*, Springer, New York (2000).
31. J. R. Cook, R. R. Bouchard, and S. Y. Emelianov, "Tissue-mimicking phantoms for photoacoustic and ultrasonic imaging," *Biomed. Opt. Express* **2**, 3193–3206 (2011).
32. Z. Zhao and R. Myllylä, "The effects of optical scattering on pulsed photoacoustic measurement in weakly absorbing liquids," *Meas. Sci. Technol.* **12**, 2172–2177 (2001).
33. E. Hecht, *Optics*, 4th ed., Chapter 9, Addison-Wesley, Reading, Massachusetts (2001).
34. C. Zhang et al., "In vivo photoacoustic microscopy with 7.6-μm axial resolution using a commercial 125-MHz ultrasonic transducer," *J. Biomed. Opt.* **17**(11), 116016 (2012).
35. G. Paltuf et al., "Photoacoustic tomography using a Mach–Zehnder interferometer as an acoustic line detector," *Appl. Opt.* **46**, 3352–3358 (2007).
36. S. A. Sujak, W. Okulski, and W. I. Gruszecki, "Organisation of xanthophyll pigments lutein and zeaxanthin in lipid membranes formed with dipalmitoylphosphatidylcholine," *Biochim. Biophys. Acta* **1509**, 255–263 (2000).
37. R. G. M. Kolkman, W. Steenbergen, and T. G. van Leeuwen, "In vivo photoacoustic imaging of blood vessels with a pulsed laser diode," *Lasers Med. Sci.* **21**, 134–39 (2006).
38. B. F. Pouet et al., "Heterodyne interferometer with two wave mixing in photorefractive crystals for ultrasound detection on rough surfaces," *Appl. Phys. Lett.* **69**, 3782–3784 (1996).
39. A. Hochreiner et al., "Photoacoustic imaging using an adaptive interferometer with a photorefractive crystal," *J. Biophotonics* **5**(7), 508–517 (2012).
40. S. Y. Ryu et al., "Combined system of optical coherence tomography and fluorescence spectroscopy based on double-cladding fiber," *Opt. Lett.* **33**(20), 2347–2349 (2008).
41. T. Berer et al., "Multimodal noncontact photoacoustic and optical coherence tomography imaging using wavelength-division multiplexing," *J. Biomed. Opt.* **20**(4), 046013 (2015).

Jonghyun Eom received his BS degree in biomedical engineering from Yonsei University and his MS degree from the Department of Medical System Engineering (DMSE) at Gwangju Institute of Science and Technology (GIST), Republic of Korea, in 2008 and 2010, respectively. Currently, he is a PhD candidate in DMSE at GIST. He is pursuing a PhD in noncontact photoacoustic imaging using an optical interferometer and its applications. His research interests include optical coherence tomography, fluorescence imaging, and optical measurements.

Seong Jun Park received his BS degree in optical engineering and communications from Gwangju University and his MS degree in the School of Information and Communications from GIST, Republic of Korea, in 2007 and 2009, respectively. He received his PhD in engineering from GIST, Republic of Korea, in 2015. Currently, he is a research fellow at the Center for Soft and Live Matter from the Institute for Basic Science.

Byeong Ha Lee received his BS and MS degrees in physics from Seoul National University, Republic of Korea, in 1984 and 1989, respectively. He received his PhD in physics from the University of Colorado at Boulder. After working as STA in Osaka National Research Institute of Japan from 1997 to 1999, he joined GIST, Republic of Korea. His current research interests are related to developing fiber optic imaging systems for biomedical applications.